Applied Physics B (2019) 125:214
https://doi.org/10.1007/s00340-019-7325-6

Applied Physics B
Lasers and Optics

Laser-induced incandescence on metal nanoparticles: validity of the Rayleigh approximation

S. Talebi-Moghaddam[1] · T. A. Sipkens[1,2] · K. J. Daun[1]

Received: 9 July 2019 / Accepted: 4 October 2019 / Published online: 24 October 2019

Abstract
Time-resolved laser-induced incandescence (TiRe-LII) is increasingly being used to characterize non-carbonaceous nanoparticles. However, there exist several measured phenomena, particularly on metal nanoparticles, that cannot be explained using traditional models. This paper shows that some of these phenomena may be due to errors caused by the Rayleigh approximation of Mie theory, which is a standard approach for modeling the spectral absorption of carbonaceous nanoparticles but is generally invalid for metal nanoparticles. Other measurement phenomena can be explained by combining Mie theory with a polydisperse particle size distribution or by considering the change in the refractive index as the nanoparticles melt. Also, the effect of the nanoparticle charge on optical properties is investigated and is found to have a negligible effect on the TiRe-LII model.

1 Introduction

The unique chemical and electromagnetic properties of metal nanoparticles [1] underlie advancements in many areas of engineering and science, including drug delivery [2], photothermal cancer therapy [3], ultra-sensitive biosensing [4], and photovoltaic devices [5]. Gas-phase synthesis routes are capable of producing industrially relevant quantities of metal nanoparticles, but, since the functionality of nanoparticles is strongly size dependent, there is a growing demand for in situ diagnostics for measuring nanoparticle size, to understand the connections between local reactor conditions and nanoparticle formation, and, ideally, to provide feedback for online control of the synthesis process. Diagnostics are also needed to assess the unintended impact of incidental metal nanoparticles on public health [6] and ecosystems [7, 8].

Time-resolved laser-induced incandescence (TiRe-LII), which is mainly used to measure the primary particle size and volume fraction of soot in combustion-related applications, is a promising diagnostic for fulfilling this need [9–11]. In this technique, a nanosecond laser pulse heats the nanoparticles within a sample volume of aerosol, and the subsequent emission (assumed to be purely incandescence) is collected at one or more wavelengths. The spectral intensity data are connected to the unknown nanoparticle volume fraction and size distribution via two coupled models: a spectroscopic model that relates the observed spectral incandescence to an instantaneous temperature of the nanoparticle ensemble, and a heat transfer model that relates the temperature decay to the nanoparticle size distribution and other thermophysical properties of interest. While much of the development of TiRe-LII has focused on soot, this technique is increasingly applied to non-carbonaceous nanoparticles, including metals [12–17], metalloids [18–20], and oxides [10, 21, 22].

Unfortunately, current measurement models cannot wholly explain some commonly observed phenomena in TiRe-LII signals. In the case of metal nanoparticles, this includes "excessive absorption" wherein an energy balance based on the peak pyrometrically inferred nanoparticle temperature suggests that the nanoparticles absorb considerably more laser energy than can be accounted for based on the laser fluence and spectral absorption cross section at the excitation wavelength, cf. Fig. 1 [23]. Excessive absorption

This article is part of the topical collection "Laser-Induced Incandescence".

✉ S. Talebi-Moghaddam
stalebim@uwaterloo.ca

[1] Department of Mechanical and Mechatronics Engineering, University of Waterloo, 200 University Ave. West, Waterloo, ON N2L 3G1, Canada

[2] Department of Mechanical Engineering, University of British Columbia, 2329 West Mall, Vancouver, BC V6T 1Z4, Canada

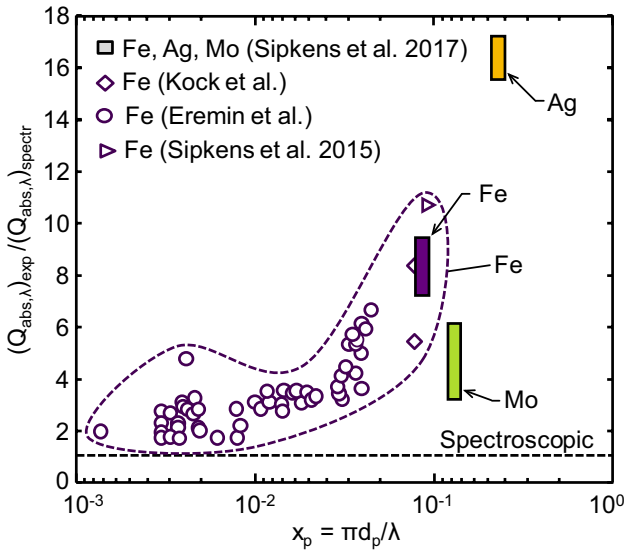

Fig. 1 Excessive absorption phenomenon in metal nanoparticles adopted from Sipkens et al. [23], including experimental data from Sipkens et al. [23], Kock et al. [25], Eremin et al. [24] and Sipkens et al. [39]. The ordinate axis is the ratio of the absorption efficiency calculated from calorimetry, $(Q_{abs,\lambda})_{exp}$ to the one predicted from the spectroscopic model, $(Q_{abs,\lambda})_{spectr}$. The spectroscopic absorption efficiency is found by using Rayleigh approximation and assuming a monodisperse aerosol with a geometric mean of the size distribution as nanoparticle size, while $(Q_{abs,\lambda})_{exp}$ is found by using the peak pyrometry effective temperature in calorimetry. The excitation wavelength in all experiments was 1064 nm

has been reported for iron, molybdenum, and silver nanoparticles [23, 24]. Moreover, TiRe-LII measurements on iron nanoparticles must be interpreted by treating the complex refractive index of iron, m_λ, as uniform [25] or nearly uniform [23] over the detection wavelengths to obtain the expected particle size distribution and peak nanoparticle temperature. This is contrary to the bulk property given in the literature, which varies significantly over the visible and near-infrared spectra. Another unexplained feature concerns the intensity scaling factor (ISF), a coefficient that relates the nanoparticle incandescence calculated using the spectral absorption cross section and the blackbody intensity to the detected incandescence signal [26]. The ISF accounts for the efficiency and configuration of the collection optics and the aerosol volume fraction; so it should, in principle, remain constant during a single shot measurement provided the laser fluence is low enough to avoid significant particle vaporization. Nevertheless, the effective ISF inferred from TiRe-LII measurements on liquid silicon nanoparticles [20], iron, molybdenum, and silver nanoparticles [27], and soot [26, 28, 29] shows that this quantity changes over time in a manner that cannot be explained by evaporation of the nanoparticle material alone.

Various hypotheses have been proposed to interpret these phenomena. Eremin et al. [24] propose a size-dependent refractive index function for carbon and iron nanoparticles to explain the excessive absorption phenomenon. However, while the apparent refractive index may become size dependent through electron scattering from the nanoparticle surface, this phenomenon only occurs for nanoparticle diameters that approach the mean free electron path, which is typically only a few nanometers [30, 31].

Alternatively, the anomalies could be explained by short-lived non-incandescent laser-induced emission (LIE) that may contaminate the incandescence signals. Non-incandescent emission could arise from a variety of sources [12], such as: stimulated emission from bulk gas molecules [7]; emission from electronically excited species vaporized from the nanoparticle [32]; chemiluminescence from reactions between the evaporated species and the nanostructures [33]; photoemission from the nanoparticles caused by non-radiative plasmon decay [34]; hot-electron intraband luminescence [35]; or broadband bremsstrahlung emission from a plasma in the gas phase caused by electron emission from the laser-irradiated nanoparticle by thermionic emission [36], thermally assisted photoemission [37], plasmonic decay photoemission [38], or other processes. The reverse process, inverse neutral bremsstrahlung, in which electrons absorb incident photons over a broad range of wavelengths as the electrons accelerate around neutral gas molecules, could also account for an enhanced absorption cross section [36].

While some or all of these phenomena may be occurring, we suggest that, for metal nanoparticles, many of these unexplained anomalies may originate from a misapplication of Rayleigh theory to model the spectral absorption cross section of the nanoparticles. Rayleigh theory has been nearly universally applied to interpret TiRe-LII measurements on non-carbonaceous nanoparticles (e.g., [11, 20, 25, 40–43]), with the justification that the size criterion is satisfied ($x_p = \pi d_p/\lambda \ll 1$). However, this rationale disregards the second criterion needed to ensure the validity of the electrostatic approximation: $|m_\lambda| x_p \ll 1$. For metal nanoparticles, $|m_\lambda|$ is usually much larger than for carbonaceous nanoparticles in the visible and near-infrared spectra, such that this criterion is generally not satisfied. In this case, the Rayleigh theory should not be applied to interpret TiRe-LII measurements. Errors induced by a misapplication of Rayleigh theory can be further exacerbated by modeling an aerosol containing polydisperse particle sizes as monodisperse, which is a common practice to simplify data analysis. Moreover, while most TiRe-LII models account for the temperature dependence of specific heat and density, radiative properties are almost always treated as invariant as the nanoparticles heat and then cool. This may be an inaccurate assumption for most metal nanoparticles, which change from solid to liquid during laser heating.

This paper investigates how applying Mie theory, incorporating polydispersity of primary particle sizes, and accounting for the change in the refractive index about the melting point, may explain anomalies in TiRe-LII measurements on metal nanoparticles. We start by introducing the spectroscopic and heat transfer models used in TiRe-LII analyses, including a summary of Mie theory as it applies to the absorption of E–M waves by silicon, iron, silver, and molybdenum nanoparticles. Synthetic signals are generated for monodisperse and polydisperse aerosols by applying Mie theory to modeled nanoparticle temperature decays. The signals are then interpreted using the Rayleigh approximation and a quadrupole approximation to Mie theory to investigate the effect that these approximations have on the inferred properties. We show that using Mie theory instead of the Rayleigh approximation and considering polydisperse particle sizes explains the discrepancy between the experimentally derived and simulated ISF and may partially explain the apparent discrepancy in the $E(m)$ ratio at the detection wavelengths for iron nanoparticles, while these effects combined with the change in refractive index when the nanoparticles melt partially accounts for the apparent enhanced absorption cross section. We also show that the nanoparticle charge state is unlikely to contribute to these anomalies. Remaining anomalies suggest that some other spectroscopic phenomena must also be occurring to explain the enhanced absorption of laser energy, particularly for silver nanoparticles.

2 TiRe-LII measurement model

2.1 Spectroscopic model

For a polydisperse, optically thin aerosol, the total spectral incandescence, J_λ, emitted by heated nanoparticles within the probe volume is found by

$$J_\lambda(t) = \Lambda \int_0^\infty p(d_\mathrm{p}) \frac{\pi d_\mathrm{p}^2}{4} Q_{\mathrm{abs},\lambda}(d_\mathrm{p}, m_\lambda) I_{\mathrm{b},\lambda}\left[T_\mathrm{p}(t, d_\mathrm{p})\right] d(d_\mathrm{p}), \tag{1}$$

where Λ is the intensity scaling factor (ISF) [26]; $I_{\mathrm{b},\lambda}$ is the blackbody spectral intensity at the nanoparticle temperature, T_p; d_p is the nanoparticle size; $p(d_\mathrm{p})$ is the instantaneous nanoparticle size distribution; and $Q_{\mathrm{abs},\lambda}$ is the spectral absorption efficiency, which is discussed further in Sect. 3. While the particle sizes in most aerosols are polydisperse, many LII studies model the aerosol as monodisperse. In this case, Eq. (1) simplifies to

$$J_\lambda(t) = \Lambda \frac{\pi d_\mathrm{p}^2}{4} Q_{\mathrm{abs},\lambda}(d_\mathrm{p}, m_\lambda) I_{\mathrm{b},\lambda}\left[T_\mathrm{p}(t, d_\mathrm{p})\right]. \tag{2}$$

Equations (1) and (2) connect the measured spectral incandescence from the probe volume, $J_\lambda(t)$, to the particle temperature. The spectral incandescence measured at two or more wavelengths is then used to infer an "effective" pyrometric temperature that is a point estimate of the distribution of nanoparticle temperatures within the probe volume at any instant. This calculation and its relationship with the spectroscopic properties of the nanoparticles are discussed further in Sect. 3. References [11, 44] provide further details on the LII spectroscopic model.

2.2 Heat transfer model

The spectroscopic model is coupled with a heat transfer model that describes how the nanoparticle temperature (which indicates its sensible energy) changes with time. For each size class, the nanoparticle temperature is found by solving

$$\frac{\pi}{6} d_\mathrm{p}^3 \rho_\mathrm{p}(t) c_\mathrm{p}(t) \frac{\mathrm{d}T_\mathrm{p}}{\mathrm{d}t} = q_\mathrm{laser}(t) - q_\mathrm{evap}\left[T_\mathrm{p}(t)\right] - q_\mathrm{cond}\left[T_\mathrm{p}(t)\right], \tag{3}$$

where ρ_p and c_p are the density and specific heat of the nanoparticle, respectively, and q_laser, q_evap and q_cond are the laser absorption, evaporation and conduction heat transfer rates, respectively. Laser heating is given by

$$q_\mathrm{laser}(t) = F_0 f(t) \frac{\pi d_\mathrm{p}^2}{4} Q_{\mathrm{abs},\lambda_\mathrm{laser}}, \tag{4}$$

where F_0 is the laser fluence, $f(t)$ is the temporal laser profile, and λ_laser is the laser wavelength. Since the diameters of the nanoparticles involved in TiRe-LII measurements are smaller than the mean free path of the buffer gas in most TiRe-LII experiments (> 1 μm), evaporation typically occurs in the free molecular (Knudsen) regime, and the evaporation heat transfer rate is given by

$$q_\mathrm{evap}(t) = \pi d_\mathrm{p}^2 N_v'' \frac{\Delta H_\mathrm{v}}{N_A}, \tag{5}$$

where ΔH_v is the molar latent heat of vaporization, N_A is Avogadro's number,

$$N_\mathrm{v}''(t) = \frac{n_\mathrm{v} v_\mathrm{v}}{4} = \frac{1}{4} \underbrace{\frac{p_\mathrm{v}}{k_B T_\mathrm{p}}}_{n_\mathrm{v}} \underbrace{\left(\frac{8 k_B T_\mathrm{p}}{\pi m_\mathrm{v}}\right)^{1/2}}_{c_\mathrm{v}} \tag{6}$$

is the number flux of evaporated molecules from nanoparticle surface, n_v and c_v are the number density (in molecules/m^3) and the mean thermal speed of the evaporated species, p_v is the vapour partial pressure of the evaporated species, k_B is Boltzmann's constant, and m_v is the molecule mass of the evaporated species. The Clausius–Clapeyron equation gives the partial pressure

$$p_\mathrm{v} = p^* \exp\left[\frac{\Delta H_\mathrm{v}\left(T_\mathrm{p} - T^*\right)}{R T_\mathrm{p} T^*}\right], \tag{7}$$

where p^* and T^* are the reference pressure and temperature, respectively, and R is the universal gas constant [43, 45]. The evaporation rate also causes the nanoparticle mass to change according to

$$\frac{\mathrm{d}m_\mathrm{p}}{\mathrm{d}t} = -\dot{m}_\mathrm{evap}\left(T, d_\mathrm{p}\right) = -m_\mathrm{v}\frac{q_\mathrm{evap}(t)}{\Delta H_\mathrm{v}} \tag{8}$$

The instantaneous nanoparticle mass is then used to calculate the nanoparticle diameter given by

$$d_\mathrm{p}(t) = \left\{\frac{6m_\mathrm{p}(t)}{\pi\rho_\mathrm{p}\left[T_\mathrm{p}(t)\right]}\right\}^{\frac{1}{3}}. \tag{9}$$

Heat conduction also occurs within the free molecular regime and is given by [23, 44]

$$q_\mathrm{cond}\left(T_\mathrm{p}, d_\mathrm{p}\right) = \pi d_\mathrm{p}^2 N_\mathrm{g}''\langle E_\mathrm{o} - E_\mathrm{i}\rangle = \pi d_\mathrm{p}^2\frac{n_\mathrm{g}c_\mathrm{g,t}}{4}\langle E_\mathrm{o} - E_\mathrm{i}\rangle, \tag{10}$$

where N_g'' is the incident gas number flux; $n_\mathrm{g} = p_\mathrm{g}/(k_B T)$ is the molecular number density of the buffer gas; $c_\mathrm{g,t} = [8k_B T_\mathrm{g}/(\pi m_\mathrm{g})]^{1/2}$ is the mean thermal speed of the carrier gas; p_g, T_g, and m_g are the carrier gas pressure, temperature, and molecular mass, respectively; $\langle E_0 – E_i\rangle$ is the average energy transfer per collision, which can be written using the thermal accommodation coefficient, α,

$$\langle E_0 - E_i\rangle = \alpha\langle E_0 - E_i\rangle_\mathrm{max} = \alpha\left(2 + \zeta_\mathrm{rot}/2\right)k_B\left(T_\mathrm{p} - T_\mathrm{g}\right), \tag{11}$$

where ζ_rot is the number of rotational degrees of freedom of the buffer gas. In the present study, we consider monatomic gases such that $\zeta_\mathrm{rot} = 0$. The conduction cooling term then reduces to

$$q_\mathrm{cond}\left(T_\mathrm{p}, d_\mathrm{p}\right) = \frac{\pi}{2}d_\mathrm{p}^2 n_\mathrm{g}c_\mathrm{g,t}\alpha k_B\left(T_\mathrm{p} - T_\mathrm{g}\right). \tag{12}$$

Other heat transfer terms, including radiation and thermionic emission, are typically much smaller than evaporation and conduction and can be excluded from the model. Further details on the LII heat transfer model can be found in Refs. [11, 44].

3 Spectral absorption efficiency of nanoparticles

3.1 Optical properties

Equations (1) and (2) highlight the importance of the spectral absorption efficiency when interpreting TiRe-LII data. Assuming that the nanoparticles are large enough to ignore electron scattering effects [30, 31], which only become important when nanoparticle diameters approach the mean free electron path of the bulk material, the spectral absorption cross section of a nanoparticle depends exclusively on two parameters: the size parameter, $x_\mathrm{p} = \pi d_\mathrm{p}/\lambda$, and the electromagnetic properties of the bulk material, expressed in terms of the complex refractive index, $m_\lambda = n_\lambda + jk_\lambda$, or complex dielectric permittivity, $\varepsilon_\lambda = \varepsilon_\mathrm{I} + j\varepsilon_\mathrm{II}$. These latter quantities are related by

$$\varepsilon_\mathrm{I} = n^2 - k^2, \varepsilon_\mathrm{II} = 2nk. \tag{13}$$

The Lorentz–Drude model can describe some metal dielectric functions. It is given by [46]

$$\varepsilon_\lambda = \underbrace{1 - \frac{f_0\omega_p^2}{\omega\left[\omega - j\Gamma_0\right]}}_{\text{Drude}} + \underbrace{\sum_{n=1}^{m}\frac{f_n\omega_\mathrm{p}^2}{\left(\omega_n^2 - \omega^2\right) + j\omega\Gamma_n}}_{\text{Lorentz}}, \tag{14}$$

where $\omega = 2\pi c_0/\lambda$ is the angular frequency of the incident wave, c_0 is the speed of light in a vacuum, ω_p is the plasma frequency of the electrons with an oscillator strength of f_n, and Γ_n is the damping coefficient, which is related to the collision frequency between electrons and atoms/ions by $\tau = 1/\Gamma_n$. The Drude term in Eq. (14) accounts for free-electron effects (intraband transitions) and the Lorentz term accounts for bound-electron effects (interband transitions).

In most LII experiments on metal aerosols reported in the literature, the nanoparticles start as a solid and melt as they are heated. Exceptions include molybdenum nanoparticles, which remain solid due to their comparatively high melting temperature, and silicon and germanium nanoparticles within a microwave plasma reactor, e.g., Ref. [19], in which the nanoparticles are in liquid state throughout the measurement. Accordingly, it is crucial to consider the electromagnetic properties of both the solid and liquid phases, which may differ significantly primarily due to changes in the electron band structure. The Drude model can also describe the optical properties of some liquid metals and metalloids, specifically those in which interband transition effects are not significant over the spectrum of interest. Values of ω_p, f_0, and Γ_0 for liquid silicon and silver are taken from Refs. [49] and [51], respectively. The refractive index of solid silver is calculated using Eq. (14) with model parameters adapted from Ref. [46]. In cases where the Drude model is not valid (iron and molybdenum [52]), the optical properties are taken from ellipsometry measurements carried out on bulk samples, with the values summarized in Table 1.

3.2 Evaluating the absorption cross section

The absorption efficiency of nanoparticles can be obtained from the optical properties of the bulk material using one of the several candidate models. Most generally, the spectral

absorption efficiency of a non-magnetic, uncharged, spherical nanoparticle embedded in a dielectric material can be found directly by Mie theory [53, 54]. In this theory, extinction and scattering efficiencies, denoted by $Q_{\mathrm{ext},\lambda}$ and $Q_{\mathrm{sca},\lambda}$, respectively, are defined as the ratios between the corresponding radiative and geometrical cross sections of the spherical particle. Assuming that the sphere is embedded within a vacuum or a medium having a refractive index of unity (e.g., most gases at visible and near-infrared), $Q_{\mathrm{ext},\lambda}$ and $Q_{\mathrm{sca},\lambda}$ are given by

$$Q_{\mathrm{ext},\lambda} = \frac{2}{x_{\mathrm{p}}^2}\sum_{l=1}^{\infty}(2l+1)Re\left(a_l + b_l\right) \tag{15}$$

and

$$Q_{\mathrm{sca},\lambda} = \frac{2}{x_{\mathrm{p}}^2}\sum_{l=1}^{\infty}(2l+1)\left(|a_l|^2 + |b_l|^2\right), \tag{16}$$

where

$$a_l = \frac{u\psi_l(uy)\psi_l'(y) - \psi_l(y)\psi_l'(uy)}{u\psi_l(uy)\xi_l'(y) - \xi_l(y)\psi_l'(uy)}, \tag{17}$$

and

$$b_l = \frac{\psi_l(uy)\psi_l'(y) - u\psi_l(y)\psi_l'(uy)}{\psi_l(uy)\xi_l'(y) - u\xi_l(y)\psi_l'(uy)} \tag{18}$$

are scattering coefficients; $u = \varepsilon_\lambda^{1/2}$; ε_λ is the relative complex permittivity of the nanoparticle; and Ψ_l and ξ_l are the Riccati–Bessel functions of order l. Finally, the spectral absorption cross section is inferred from

$$Q_{\mathrm{abs},\lambda} = Q_{\mathrm{ext},\lambda} - Q_{\mathrm{sca},\lambda}. \tag{19}$$

While Mie theory provides an exact solution to the spectral absorption coefficient of spherical nanoparticles, it is rarely used to analyze LII data due to the computational effort associated with evaluating the Riccati–Bessel functions and because it requires knowledge of the nanoparticle diameter, which is typically unknown and the focus of the LII analysis.

Instead, practitioners use an approximation for the absorption cross section. Invoking the electrostatic approximation, in which the variation of the electromagnetic field inside the nanoparticle is assumed to be negligible at any instant, is tantamount to neglecting the influence of electromagnetic field coupling [54]. This results in the Rayleigh approximation to Mie's equations, in which

$$Q_{\mathrm{abs},\lambda} = 4x_{\mathrm{p}}E\left(m_\lambda\right), \tag{20}$$

where

$$E\left(m_\lambda\right) = \mathrm{Im}\left(\frac{m_\lambda^2 - 1}{m_\lambda^2 + 2}\right) \tag{21}$$

is the absorption function. This approach is appealing for two reasons: (1) this model is far simpler and much less computationally expensive to implement compared to the full Mie equations, and (2) the electrostatic assumption separates the influence of the bulk electromagnetic (m_λ or ε_λ) and size ($x_{\mathrm{p}} = \pi d_{\mathrm{p}}/\lambda$) on $Q_{\mathrm{abs},\lambda}$. Consequently, the peak effective temperature derived from the TiRe-LII data is nearly independent of size, and, for the monodisperse case, the spectroscopic and heat transfer submodels can be decoupled and solved sequentially. For these reasons, the Rayleigh approximation is almost universally applied to analyze LII data.

The validity of the Rayleigh approximation relies on two criteria: (1) $x_{\mathrm{p}} \ll 1$, and (2) that the phase shift parameter satisfies $x_{\mathrm{p}}|m_\lambda| \ll 1$. While the latter criterion is usually satisfied for carbonaceous nanoparticles (e.g., soot), this is not true for metal nanoparticles since they have a much larger refractive index, as shown in Fig. 2. Consequently, the internal electric field of the nanoparticle during wave interaction is not sufficiently uniform to be approximated by a single dipole for the wavelengths important to LII. This finding conflicts somewhat with a recent paper by Sorensen et al. [56], who downplay the importance of the phase shift criteria because, they argue, absorption is an incoherent phenomenon. They also suggest that all spheres, regardless of size, display semi-quantitative Rayleigh behaviour for the condition $x_{\mathrm{p}} \cdot k < 0.3$. However, their study assumes a fixed value of $n = 1.5$, which is much smaller than values typical of metals in the visible and near-infrared and ignores the fundamental correlation between k and n through the plasmon frequency and electron damping coefficient—moreover, the Mie absorption, Eq. (19), is a linear combination of Mie scattering coefficients a_l and b_l which depend on both n and k through $u = (\varepsilon_{\mathrm{p}})^{1/2} = m_\lambda$. This can be shown by examining the difference between Rayleigh and Mie absorption efficiency predictions and the phase shift parameter over a range of n and k values expected for non-plasmonic metal

Table 1 Refractive index of metal nanoparticles examined in this work

Material	$\lambda = 442$ nm	$\lambda = 716$ nm	$\lambda = 1064$ nm
Fe (solid, 30 °C) [47]	$2.54 + 2.74\,j$	$2.86 + 3.21\,j$	$2.93 + 3.99\,j$
Fe (liquid, 1616 °C) [48]	$2.37 + 3.21\,j$	$3.48 + 4.13\,j$	$5.64 + 5.01\,j$
Si (liquid, 1414 °C) [49]	$2.11 + 4.53\,j$	$3.58 + 5.95\,j$	$5.06 + 7.18\,j$
Mo (solid, 1926 °C) [50]	$2.83 + 3.45\,j$	$3.83 + 4.09\,j$	$4.29 + 5.30\,j$
Ag (solid, 30 °C) [46]	$0.14 + 2.25\,j$	$0.16 + 4.42\,j$	$0.24 + 6.87\,j$
Ag (liquid, 962 °C) [51]	$0.10 + 2.92\,j$	$0.25 + 4.89\,j$	$0.55 + 7.31\,j$

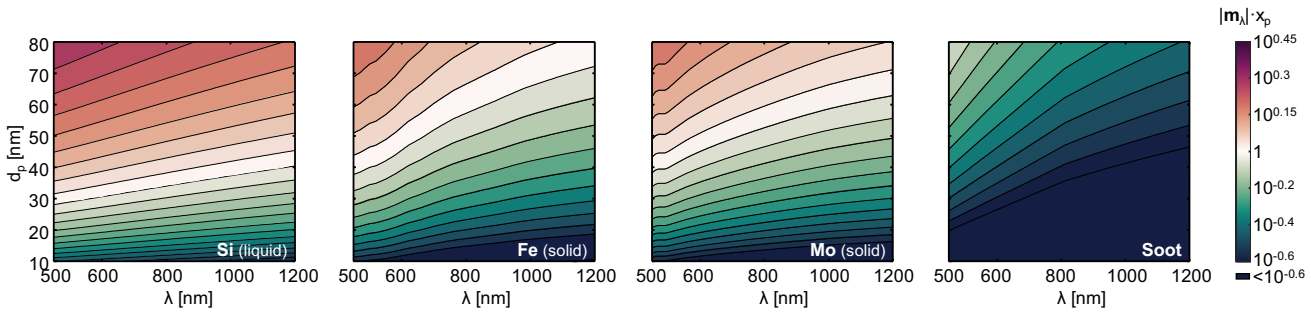

Fig. 2 Comparison of $|m_\lambda|x_p$ values for different nanoparticles. Contours are logarithmic. The lightest region represents those values close to $|m_\lambda|x_p = 1$, and Rayleigh theory is expected to valid in those regions that are dark blue (bottom right corner of most plots). The refractive index of soot is adopted from Ref. [55]

nanoparticles at 1064 nm ($n \in [1, 7]$, $k \in [1, 7]$). These differences are highly correlated with the phase shift parameter (Pearson correlation coefficients greater than 90% for nanoparticles with $d_p < 100$ nm), which can, thus, be used as an error metric.

The shortcomings of the Rayleigh approximation present a need for other $Q_{abs,\lambda}$ models that are more accurate but avoid the complexity and computational effort of the full Mie solution. Schebarchov et al. [57] recently presented a simple, computationally efficient, closed-form approximation to the exact Mie solution for metal nanospheres under 100 nm:

$$Q_{ext}^{Mie,approx} = -\frac{2}{x_p^2} Re\left[3b_1 + 3a_1 + 5b_2 + O\left(x_p^7\right)\right] \tag{22}$$

and

$$Q_{sca}^{Mie,approx} = \frac{2}{x_p^2}\left[3|b_1|^2 + 3|a_1|^2 + 5|b_2|^2 + O\left(x_p^7\right)\right]. \tag{23}$$

The extinction and scattering efficiencies can be approximated using the scattering coefficients, a_1 and b_1, as defined above. Equations (22) and (23) predict scattering and absorption spectra of metal nanospheres and account for localized surface plasmon resonances (LSPR) which depends mostly on b_1 (electric dipole), b_2 (electric quadrupole) and a_1 (magnetic dipole). The electric quadrupole, b_2, and magnetic dipole, a_1, contributions are of the order x_p^5. The remaining truncated terms are of order x_p^7 or higher.

3.3 Defining the effective temperature and intensity scaling factor

Most often, the raw TiRe-LII data are converted into an effective temperature via a calibration (which relates the raw data to spectral incandescence measurements) and then a spectroscopic model, cf. Eq. (2). This approach is appealing for several reasons: it reduces the dimension of the inference problem; it avoids the need to infer the intensity scaling factor, which relates the measured LII signal to the spectral incandescence [26]; and it gives a temperature that provides some physical insight into the heat transfer processes that govern nanoparticle heating and cooling. In general, one can define an effective temperature at any given instant in time using a least squares analysis by assuming that all the detected radiation is due to nanoparticle incandescence,

$$x(t) = \begin{bmatrix} T^{eff}(t) \\ \Lambda^{eff}(t) \end{bmatrix} = \arg\min_{T,\Lambda} \left\{ \left\| \begin{matrix} J_{\lambda_1} - \Lambda \cdot Q_{abs,\lambda_1} \cdot I_{b,\lambda_1}(T) \\ \vdots \\ J_{\lambda_w} - \Lambda \cdot Q_{abs,\lambda_w} \cdot I_{b,\lambda_w}(T) \end{matrix} \right\|_2^2 \right\}. \tag{24}$$

In the above equation, all the terms are time dependent, including the ISF and absorption efficiency. If Rayleigh theory is used to model $Q_{abs,\lambda}$, the inference becomes

$$x^{Rayl} = \begin{bmatrix} T^{eff,Rayl} \\ \Lambda^{eff,Rayl} \end{bmatrix} = \arg\min_{T,\Lambda} \left\{ \left\| \begin{matrix} J_{\lambda_1} - \Lambda \cdot E(m_{\lambda 1}) \cdot I_{b,\lambda_1}(T) \\ \vdots \\ J_{\lambda_w} - \Lambda \cdot E(m_{\lambda 1}) \cdot I_{b,\lambda_w}(T) \end{matrix} \right\|_2^2 \right\}. \tag{25}$$

The $\pi d_p^2/4$ and $\pi d_p^3/\lambda$ terms are merged into Λ coefficient in Eqs. (24) and (25), respectively. For the particular case of two-color pyrometry ($w = 2$), a closed-formed solution for T^{eff} is found by invoking Wien's approximation and taking the ratio of the signals

$$T^{eff,Rayl}(t) = \frac{hc_0}{k_B}\left(\frac{1}{\lambda_1} - \frac{1}{\lambda_2}\right)\left[\ln\left(\frac{J_{\lambda 1}(t)}{J_{\lambda 2}(t)}\frac{1}{E(m)_r}\left(\frac{\lambda_1}{\lambda_2}\right)^6\right)\right]^{-1}, \tag{26}$$

and $E(m)_r = E(m_{\lambda 1})/E(m_{\lambda 2})$. This avoids calculating the ISF altogether, although the parameter can still be evaluated by substitution and contains useful information [26].

If one cannot invoke the Rayleigh approximation, the absorption cross section is a non-linear function of the nanoparticle diameter. Accordingly, defining an effective temperature now requires knowledge of d_p, which is not generally known a priori. One solution is to also define an

effective diameter, $d_{p,eff}$, which can then used to define an effective temperature,

$$x^{\mathrm{Mie}}\left(d_{p,\mathrm{eff}}\right) = \begin{bmatrix} T^{\mathrm{eff,Mie}}\left(d_{p,\mathrm{eff}}\right) \\ \Lambda^{\mathrm{eff,Mie}}\left(d_{p,\mathrm{eff}}\right) \end{bmatrix} = \arg\min_{T,\Lambda} \left\{ \left\| \begin{matrix} J_{\lambda_1} - \Lambda \cdot Q_{\mathrm{abs},\lambda_1}\left(d_{p,\mathrm{eff}}\right) \cdot I_{b,\lambda_1}(T) \\ \vdots \\ J_{\lambda_w} - \Lambda \cdot Q_{\mathrm{abs},\lambda_1}\left(d_{p,\mathrm{eff}}\right) \cdot I_{b,\lambda_1}(T) \end{matrix} \right\|_2^2 \right\}. \tag{27}$$

This effective temperature corresponds to an ensemble average of the temperatures in the real aerosol and represents the temperature of a hypothetical monodisperse aerosol of the specified effective diameter that will produce an emission spectrum that most closely resembles the experimental emission spectrum. An identical treatment must be applied to simulated data to infer the effective temperature. One candidate effective diameter is the geometric mean, $d_{p,g}$, which is motivated by the fact that, when using Rayleigh theory to interpret laser absorption and incandescence from nanoparticles during conduction-dominated cooling, the pyrometric temperature would correspond to that of a hypothetical monodisperse aerosol containing nanoparticles having the geometric mean diameter of the polydisperse aerosol [58]. Alternatively, the volumetric diameter

$$d_{p,v} = \left(\int_0^\infty d_p^3 p\left(d_p\right) \mathrm{d}d_p \right)^{1/3} \tag{28}$$

could be used.

The pyrometric temperature is often used to indicate the internal energy of the atoms and molecules in the nanoparticle, and the variation of peak pyrometric temperature with laser fluence is often related to evaporation and sublimation. If exact nanoparticle size distribution and corresponding size-dependent temperatures are known, the instantaneous thermodynamic temperature (i.e., the temperature that indicates the average internal energy of the nanoparticles within the probe volume) could be calculated from

$$T^{\mathrm{thermo}} = \frac{\int_0^\infty T\left(d_p\right) c_p \rho d_p^3 p\left(d_p\right) \mathrm{d}d_p}{\int_0^\infty c_p \rho d_p^3 p\left(d_p\right) \mathrm{d}d_p}, \tag{29}$$

where as before, all of the terms can be a function of time.

4 Effect of the spectroscopic model assumptions on TiRe-LII data interpretation

Consider now the kind of errors that will result if the Rayleigh approximation is used to simulate the incandescence signals.

4.1 Effect of the spectroscopic model assumptions on the simulated nanoparticle temperature

Most TiRe-LII analyses assume that nanoparticles are heated to the same peak temperature regardless of their size, a consequence of the fact that the Rayleigh absorption cross section and the sensible energy of the nanoparticle are both proportional to d_p^3. Consider simulated LII measurements on liquid silicon nanoparticles generated using model parameters adapted from Menser et al. [20]. Nanoparticles are heated using a spatially uniform and temporally Gaussian pulse at 1064 nm with a full-width half-maximum of 15 ns at a fluence of 8 mJ/mm^2. The bath gas consists of 93% Ar and 7% H_2 at $T_g = 1500$ K and $P_g = 10$ kPa, and $\alpha = 0.2$ is assumed for the heat transfer model. Figure 3a shows that the Rayleigh model predicts an approximately identical temperature profile for nanoparticles of different sizes, with the only differences stemming from a size-dependent nanoparticle dilation due to the temperature-dependent density, and a size-dependent evaporation rate. In contrast, Mie theory predicts a much broader range in peak temperatures, which results in a strong size-dependent decay rate in the nanoparticle temperature following the peak temperature, with large nanoparticles exhibiting rapid mass loss due to evaporation, cf. Fig. 3b. This would result in significant errors that would propagate into inferred nanoparticle diameters. The quadrupole approximation, Eqs. (22) and (23), generally overpredicts the absorption cross section of larger nanoparticles, increasing the range of modeled peak temperatures, cf. Fig. 3c. Consequently, more mass loss is predicted for larger nanoparticles due to superheating relative to Mie theory, especially during the laser pulse period.

4.2 Effect of the spectroscopic model assumptions on the prompt effective temperature

Consider the Mie theory results shown in Fig. 3b as the ground truth. Incandescence signals are generated by integrating the incandescence emitted by each size class over a lognormal distribution having a geometric mean and standard deviation of 25 nm and 1.3, respectively, following Eq. (1). Spectral signals are generated by sampling the incandescence between 425 nm and 700 nm at 0.4 nm intervals, matching the resolution of the spectrometer used in Ref. [20]. The simulated incandescence signals are then used to calculate an effective temperature using either (1) the Rayleigh approximation, Eq. (25), or (2) Mie theory with $d_{p,g}$ or $d_{p,v}$ as effective diameter, Eq. (27). Fig. 4 shows that the effective temperature obtained from the Rayleigh interpretation closely resembles the thermodynamic temperature and that the Rayleigh- and Mie-based

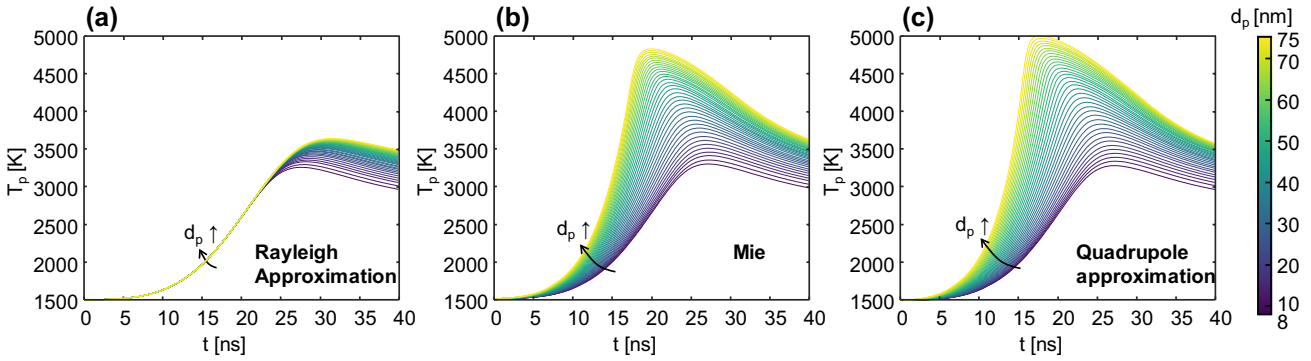

Fig. 3 Temperature of liquid silicon nanoparticles obtained using a laser having a uniform spatial and Gaussian temporal profile. Results are shown for a range of spectroscopic models, including: **a** the Rayleigh approximation, Eq. (20); **b** Mie theory; Eqs. (15) and (16); and **c** the quadrupole approximation [57], Eq. (22)

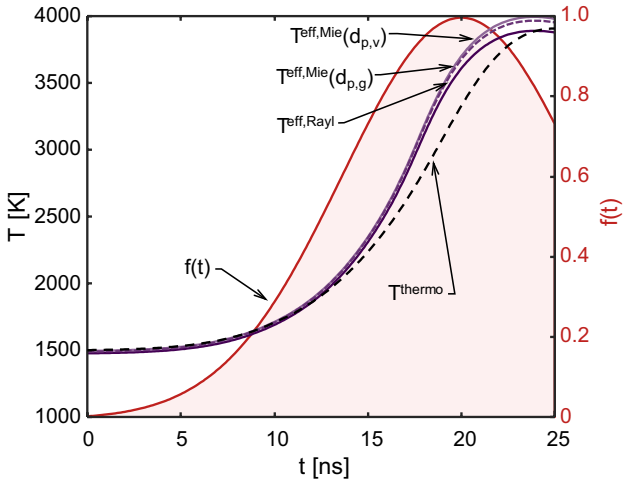

Fig. 4 The effective temperature of silicon nanoparticles inferred by simulating the incandescence signal (using Mie theory and considering polydispersity) over a wavelengths between 425 and 700 nm. Effective temperatures are evaluated using the Rayleigh approximation, Mie theory assuming $d_{p,g}$, and Mie theory assuming $d_{p,v}$. The laser fluence, $f(t)$, is shown as a red line. The cross sections predicted using Rayleigh and Mie theory produce very similar effective temperatures, all of which exceed the thermodynamic temperature during laser heating

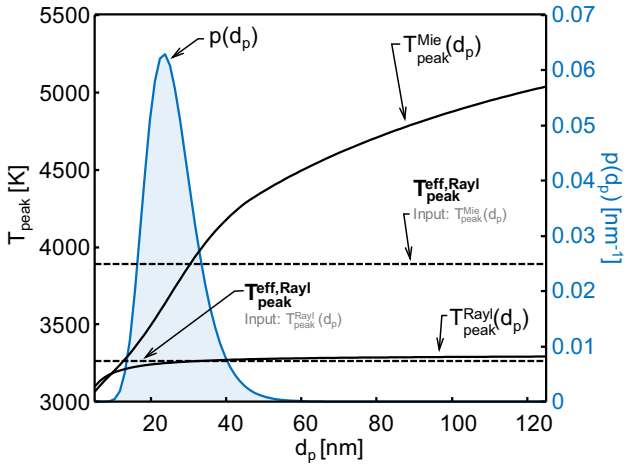

Fig. 5 Pyrometric temperature of silicon nanoparticles at the peak incandescence as a function of nanoparticle diameter, calculated using either Mie theory, $T^{Mie}_{peak}(d_p)$, or Rayleigh theory, $T^{Rayl}_{peak}(d_p)$, to generate the incandescence. (These temperatures closely correspond to the maximum temperature reached by each size class in Fig. 3a, b). Dashed horizontal lines correspond to the pyrometrically defined peak effective temperature inferred assuming Rayleigh theory (that is $T^{eff,Rayl}_{peak}$ from Eq. (25)) for incandescence generated using both methods and assuming the particle size distribution

temperatures are quite similar. This suggests that it may be reasonable to use the Rayleigh/monodisperse approximation to calculate a pyrometric temperature, even if the phase shift criterion is violated.

Figure 5 shows the nanoparticles temperature distribution at the peak incandescence signal when the absorption efficiency is calculated: (1) using Rayleigh approximation, $T^{Rayl}_{peak}(d_p)$; and (2) using Mie theory, $T^{Mie}_{peak}(d_p)$. The simulation assumptions are identical to what is used to generate Fig. 3. As previously discussed, the peak temperature predicted using Rayleigh theory is more uniform compared to Mie theory. The $T^{Rayl}_{peak}(d_p)$ and $T^{Mie}_{peak}(d_p)$ distributions are then used to define a pyrometric temperature using the Rayleigh approximation, Eq. (25), to process the total incandescence signal calculated using $p(d_p)$ in Eq. (1). The error in predicting the peak temperature distribution, $T^{Mie}_{peak}(d_p) - T^{Rayl}_{peak}(d_p)$ caused by the Rayleigh approximation, propagates into the pyrometric temperature through the modeled incandescence signal. Furthermore, this error increases as the distribution becomes wider or as it shifts towards larger particles. Therefore, we expect that the pyrometric temperature difference further increases by increasing the geometric mean or geometric standard deviation in $p(d_p)$.

4.3 Anomalies in the intensity scaling factor

Next, consider the anomalies in the effective ISF for TiRe-LII measurements on silicon nanoparticles reported by Menser et al. [20]. Effective temperatures and ISFs are evaluated using Rayleigh theory and shown as circles in Fig. 6b. While one would expect the effective ISF to be constant, analysis of experimental data shows that it varies with time, and decreases sharply after the laser pulse. Menser et al. [20] attributed this trend, in part, to the fact that the streak camera data are "temporally blended" due to the finite width of the spectrograph slit. To understand the origin of this anomaly, we simulate the incandescence signal using Eq. (1), and progressively relax a range of assumptions in the spectroscopic model used to generate the signal. In all cases, Rayleigh theory is used to calculate the effective temperature from the simulated LII signals. The TiRe-LII data is produced following three scenarios: (1) Rayleigh theory for an aerosol composed of silicon nanoparticles having a diameter of 25 nm (matching the assumptions in the pyrometric model); Mie theory with a diameter of 25 nm; (2) Mie theory with polydisperse particle diameters (lognormal with a geometric mean and standard deviation of 25 nm and 1.3, respectively); and finally (3) with the quadrupole approximation, Eq. (22), with polydisperse particle diameters.

The pyrometrically inferred effective ISF, shown in Fig. 6, changes with the assumptions used to generate the TiRe-LII signals. Using Mie theory to model the laser absorption leads to a higher mass loss due to evaporation and a larger drop in the ISF. Including polydisperse particle sizes exacerbates this effect, since polydispersity broadens the distribution of nanoparticle temperatures, cf. Section 4.1. The resulting temporal variation in the ISF closely resembles the experimental trends reported by Menser et al. [20], suggesting that this effect can be attributed mostly to the use of the Rayleigh absorption cross section combined with the assumption of monodisperse particle diameters.

These results indicate the need to couple the heat transfer and spectroscopic models for metal aerosols. While this approach was previously necessary to simulate polydispersity during nanoparticle cooling using the Rayleigh model (e.g. [19]), the results shown in Fig. 6 indicate that, for aerosols of metal nanoparticles, Mie theory should be used to model both nanoparticle heating and cooling, to capture the nanoparticle temperature distribution at any instant. Fig. 7 demonstrates the necessary steps for such an approach. Incandescence is simulated using the heat transfer and spectroscopic models, in this case evaluating the absorption efficiency using Mie theory, incorporating polydisperse sizes, and accounting for the change in the refractive index due to melting. At this point, simulated and modeled incandescence traces can be reduced to an effective temperature using Rayleigh theory, Eq. (25). The analysis then focuses on identifying the unknown aerosol attributes (e.g., size distribution parameters) by regressing the modeled effective temperatures to the measured effective temperatures, e.g., through Bayesian inference [59].

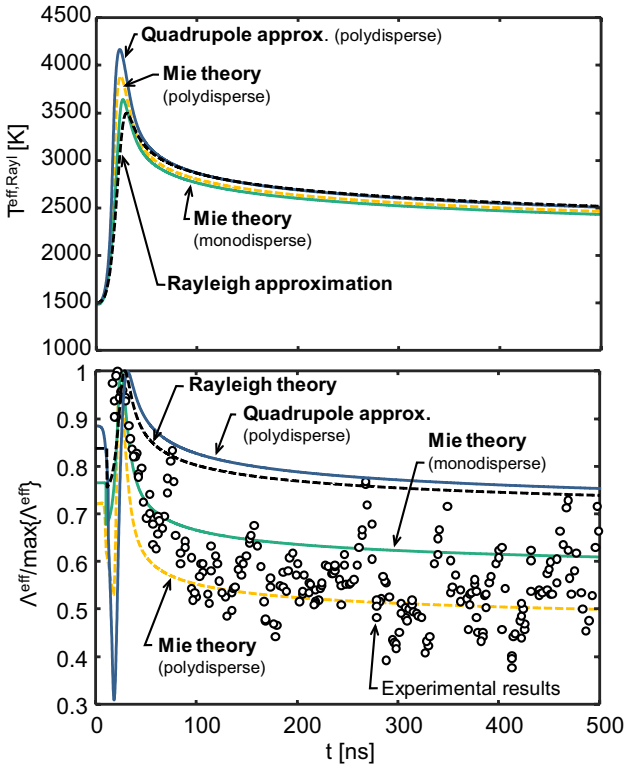

Fig. 6 Comparing the normalized effective intensity scaling factor, $\Lambda^{eff}/max(\Lambda^{eff})$, and temperature, $T^{eff,Rayl}$, (*i*) inferred using Rayleigh theory, Eq.(25), after simulating the TiRe-LII signals using different spectroscopic models, and (*ii*) reported directly by Menser et al. [20]. Simulations model liquid silicon nanoparticles with $T_g = 1500$ K, $P_g = 100$ kPa, $\alpha = 0.2$, and nanoparticles sizes approximated with a lognormal size distribution having a geometric mean and standard deviation of 25 nm and 1.3, respectively. The nanoparticles are heated using a spatially uniform and temporally Gaussian pulse at 1064 nm with a full-width half-maximum of 15 ns and a fluence of 8 mJ/mm^2

The major drawbacks of this approach are that: (1) calculation of the pyrometric temperature now requires knowledge of the particle size; and (2) the Mie absorption cross section is computationally costly to evaluate. The first issue is unavoidable as the above analysis shows that, in the case of metal aerosols, accurate TiRe-LII traces can only be generated if Mie theory is used to simulate incandescence. One may be tempted to circumvent the second issue using the Mie quadruple approximation, Eq. (22). Surprisingly, Fig. 6 shows that, when the simulated data are generated with the quadrupole approximation, the pyrometric temperature and ISF differ significantly from those found using Mie theory. As shown in Fig. 3c, the quadrupole approximation over-predicts the absorption cross section of the nanoparticle, causing the largest nanoparticles to lose a significant

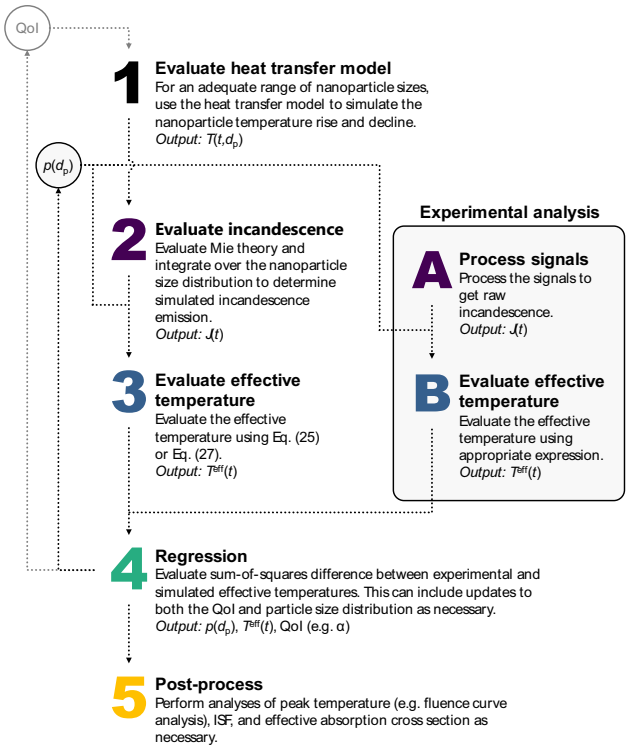

Fig. 7 Algorithm for inferring nanoparticle quantities of interest (QoI) from TiRe-LII signals for coupled spectroscopic and heat transfer models. In this instance, the particle size distribution is used to evaluate the effective temperature from both simulated and experimental incandescence (i.e., steps 3 and B). In addition, the heat transfer and spectroscopic models in steps 1 and 2 are updated to incorporate the size-dependent absorption cross section predicted by Mie theory and a change in the refractive index when the particle melts

percentage of their mass before the peak laser intensity and therefore, less mass is lost after the peak compared to the Mie theory. This effect can be seen as a sharp drop in ISF during the heating process in Fig. 6. This results in an under-prediction of $\Lambda^{\mathrm{eff}}(t)$ after the signal peak. This finding indicates that the quadrupole approximation should not be used to interpret TiRe-LII measurements on metal nanoparticles.

4.4 Peak nanoparticle temperature and excessive absorption

Another anomaly reported in the literature concerns the effective absorption cross section required for metal nanoparticles to reach the inferred peak temperature at a given laser fluence. Previous treatments by Eremin et al. [24] and Sipkens et al. [23, 39] assumed a monodisperse aerosol and determined this quantity by considering the integration of the energy balance in Eq. (3) carried out from the start of laser heating until the peak pyrometric temperature, neglecting the cooling terms,

$$\rho\left(T_{\mathrm{g}}\right)\frac{\pi d_{\mathrm{p}}^3}{6}\left[H^{\circ}\left(T_{\mathrm{peak}}^{\mathrm{eff}}\right)-H^{\circ}\left(T_{\mathrm{g}}\right)\right]\approx Q_{\mathrm{laser}}, \tag{30}$$

where $H^{\circ}(T_{\mathrm{g}})$ and $H^{\circ}(T_{\mathrm{peak}}^{\mathrm{eff}})$ are the enthalpies of the material at the buffer gas temperature, T_{g}, and the peak effective temperature, $T_{\mathrm{peak}}^{\mathrm{eff}}$, and Q_{laser} is the total energy transferred to the nanoparticle due to laser absorption throughout the laser pulse. The total laser absorption at a given fluence is

$$Q_{\mathrm{laser}}=F_0\frac{\pi d_{\mathrm{p}}^2}{4}Q_{\mathrm{abs},\lambda_{\mathrm{laser}}}. \tag{31}$$

If the nanoparticle absorption cross section is modeled using Rayleigh theory, the total absorbed laser energy is

$$Q_{\mathrm{laser}}=F_0\frac{\pi^2 d_{\mathrm{p}}^3}{\lambda_1}E\left(m_\lambda\right). \tag{32}$$

This expression can now be used to derive an effective "calorimetric" $E(m_\lambda)$ that would be necessary to reach the experimentally derived peak effective temperature,

$$\left[E\left(m_\lambda\right)\right]_{\mathrm{exp}}=\frac{\lambda_1}{6\pi F_0}\rho\left(T_{\mathrm{g}}\right)\left[H^{\circ}\left(T_{\mathrm{peak}}^{\mathrm{eff}}\right)-H^{\circ}\left(T_{\mathrm{g}}\right)\right]. \tag{33}$$

The nanoparticle size now cancels out in Eq. (33). Sipkens et al. [23, 39] defined the ratio of the calorimetrically defined absorption efficiency to the one predicted using the spectroscopic model, which, assuming Rayleigh theory and an aerosol of uniform particle sizes, amounts to

$$\frac{\left(Q_{\mathrm{abs},\lambda_{\mathrm{laser}}}^{\mathrm{eff}}\right)_{\mathrm{exp}}}{\left(Q_{\mathrm{abs},\lambda_{\mathrm{laser}}}^{\mathrm{eff}}\right)_{\mathrm{spectr}}}=\frac{\left[E\left(m_\lambda\right)\right]_{\mathrm{exp}}}{\left[E\left(m_\lambda\right)\right]_{\mathrm{spectr}}}, \tag{34}$$

where $E(m_\lambda)_{\mathrm{spectr}}$ is derived from the optical properties given in the literature.

Figure 1 shows the quantity in Eq. (34) derived from the TiRe-LII signals of Eremin et al. [24] and Sipkens et al. [23]. Eremin et al. [24] investigated aerosols of iron nanoparticles having lognormal size distributions with geometric means that varied between 2 and 15 nm and a geometric standard deviation of 1.2. TiRe-LII measurements were carried out using a 1064-nm laser at fluences between 3 and 5 mJ/mm^2 and a full-width half-maximum (FWHM) of 12 ns. Sipkens et al. [23] considered an aerosol of iron nanoparticles having diameters that obeyed a lognormal distribution with a geometric mean and standard deviation of 40 nm and 1.16, respectively; an aerosol of silver nanoparticles having diameters that obeyed a Weibull distribution with a mean of 64.4 nm and a standard deviation of 6.11; and an aerosol of molybdenum nanoparticles, having diameters that obeyed a lognormal distribution with a geometric mean and standard

deviation of 45 nm and 1.49, respectively. Fig. 1 demonstrates that the experimentally derived cross section greatly exceeds that predicted by Rayleigh theory, in some cases by more than an order-of-magnitude.

To examine this anomaly, we revisit the assumptions that underlie this calculation. For each of these cases, we generate simulated TiRe-LII signals using Mie theory and account for polydispersity and a change in the refractive index when the nanoparticles melt. The melting effect on the refractive index is assumed to be spontaneous for iron nanoparticles and is calculated using the information in Table 1. If we consider how polydispersity and variation in thermophysical properties of the nanoparticles with temperature affect the change in the internal energy of the nanoparticles, a more accurate version of the LHS of Eq. (30) is

$$U_{\mathrm{peak}} - U_0 = \int_0^\infty \left\{ \rho\left[T\left(d_{\mathrm{p}}, t_{\mathrm{peak}}\right)\right] \frac{\pi d_{\mathrm{p}}^3}{6} H^{\circ}\left[T\left(d_{\mathrm{p}}, t_{\mathrm{peak}}\right)\right] \right\} p\left(d_{\mathrm{p}}, t_{\mathrm{peak}}\right) \mathrm{d}d_p - \int_0^\infty \left\{ \rho\left(T_{\mathrm{g}}\right) \frac{\pi d_{\mathrm{p}}^3}{6} H^{\circ}\left(T_{\mathrm{g}}\right) \right\} p\left(d_{\mathrm{p}}, t_0\right) \mathrm{d}d_p, \tag{35}$$

where $p(d_{\mathrm{p}}, t_0)$ and $p(d_{\mathrm{p}}, t_{\mathrm{peak}})$ are the initial particle size distributions and the size distribution at the peak pyrometric temperature, the latter determined by solving Eq. (3), and U_{peak} and U_0 are the total internal energy of the aerosolized particle at the peak and prior to the laser pulse, respectively. By combining Eqs. (31) and (35) about the geometric mean diameter, the experimentally derived absorption efficiency can be defined as

$$\left(Q_{\mathrm{abs},\lambda_{\mathrm{laser}}}^{\mathrm{eff}}\right)_{\mathrm{exp}} \equiv \frac{4\left[U_{\mathrm{peak}} - U_0\right]}{\pi F_0 d_{\mathrm{p,g}}^2}. \tag{36}$$

This value can be compared to the one found from $[E(m_\lambda)]_{\mathrm{exp}}$ following the previous treatment by Eremin et al. [24] and Sipkens et al. [23] by evaluating

$$\left(Q_{\mathrm{abs},\lambda_{\mathrm{laser}}}^{\mathrm{eff}}\right)_{\mathrm{exp}} = \frac{4\pi d_{p,g}}{\lambda}\left[E\left(m_\lambda\right)\right]_{\mathrm{exp}}. \tag{37}$$

Applying this approach to silicon nanoparticles (using the same simulation parameters as Sect. 4.1) shows that the error caused by neglecting polydisperse particle sizes is less than 5%, cf. Table 2. Therefore, Eq. (30) can be used as a physical approximation of aerosol absorption for both simulating data and for interpreting experiments results.

With this in mind, the experimentally derived effective absorption cross section, $\left(Q_{\mathrm{abs},\lambda_{\mathrm{laser}}}^{\mathrm{eff}}\right)_{\mathrm{exp}}$, is found by multiplying the data in Fig. 1 by the spectroscopically derived Rayleigh absorption cross section at $d_{\mathrm{p,g}}$. The ratio can now be updated using a new spectroscopically derived absorption cross section obtained from the particle size distribution found using the algorithm depicted in Fig. 7. Progressively, more elaborate spectroscopic models can be used to simulate the laser heating of the nanoparticle and the emitted spectral incandescence. One should note that, according to Fig. 7, the effective absorption cross section used to define T^{eff} does not matter, as long as the simulated and measured signals are processed in the same way.

For aerosols of iron nanoparticles, Fig. 8 shows the ratio of calorimetrically derived $\left(Q_{\mathrm{abs},\lambda_{\mathrm{laser}}}^{\mathrm{eff}}\right)_{\mathrm{exp}}$, reported by Eremin et al. [15] (originally in terms of an effective $E(m_\lambda)$) to the one predicted using various spectroscopic models to compute the laser absorption and spectral incandescence, including when: (1) the absorption cross section is modelled using Mie theory and a monodisperse size distribution is assumed; (2) Mie theory is used, accounting for polydisperse sizes; and, finally, (3) one that accounts for the change in refractive index as the iron nanoparticles melt. The agreement between the experimental results and the modelled data improve considerably as additional effects are included in the simulation, largely resolving the discrepancy between spectroscopic and calorimetric absorption cross sections. Closer inspection of Fig. 8 suggests a possible size dependence for larger nanoparticles, although it is unclear whether this is significant in view of experimental uncertainties.

We repeat this analysis using calorimetrically inferred absorption cross sections for the iron, silver, and

Table 2 Comparing different effective absorption cross sections inferred from simulated data, given in Fig. 3b

Case	1	2	3
Method of calculating T^{eff}	Rayleigh, Eq. (25)	Mie, Eq. (27)	N/A
Expression to evaluate $(Q_{\mathrm{abs},\lambda})_{\mathrm{exp}}$	Eq. (37)	Eq. (37)	Eq. (36)
Includes polydispersity?	No (evaluated at $d_{\mathrm{p,g}}$)	No (evaluated at $d_{\mathrm{p,g}}$)	Yes
$(Q_{\mathrm{abs},\lambda})_{\mathrm{exp}}$	0.0113	0.0116	0.0119

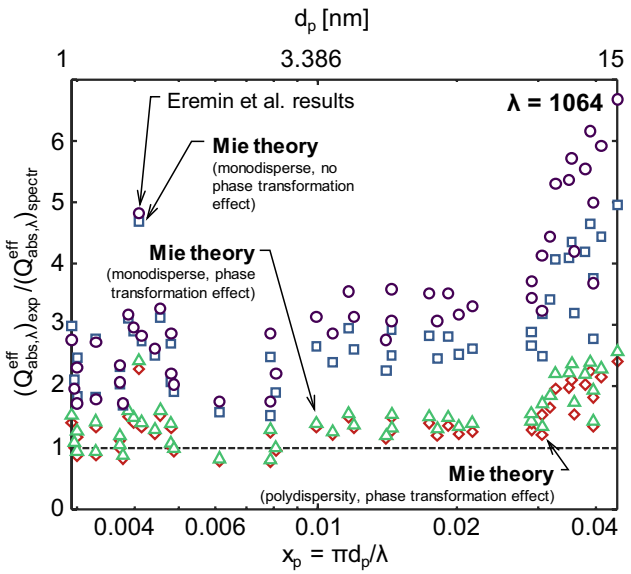

Fig. 8 Ratio of the calorimetric and spectroscopic absorption cross sections at the laser wavelength reported by Eremin et al. [24] for aerosols of solid iron nanoparticles. Purple circles are the original results calculated by comparing effective experimental absorption cross section found from Eq. (34) using the peak pyrometric temperature, compared to the Rayleigh absorption cross section at $d_{p,g}$, Eq. (20). The blue squares denote signals computed with Mie theory assuming a monodisperse aerosol ($d_p = d_{p,g}$) and ignoring the change in refractive index due to melting, and then inferring the effective absorption cross section using Eq. (33). Green triangles are found by simulating the signals using Mie for a monodisperse aerosol but with considering the refractive index change due to melting. Red diamonds show results by considering Mie theory, polydispersity and refractive index change due to melting, which is the most accurate model. The largest effect comes from considering the change in refractive index upon melting, and, for larger nanoparticles, Mie theory and polydisperse sizes

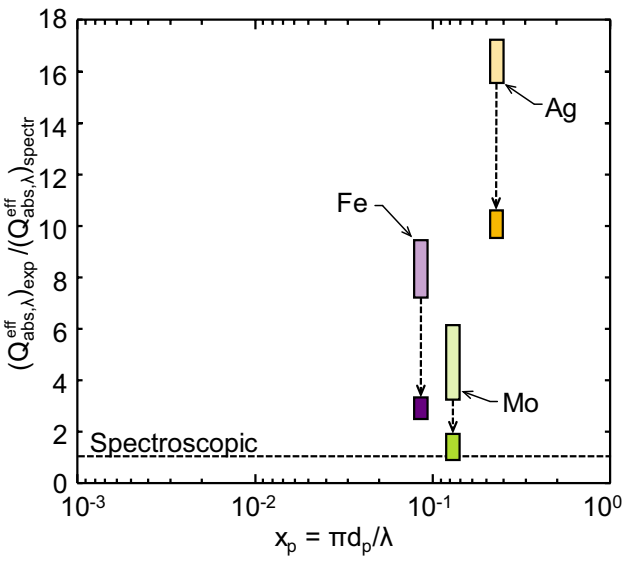

Fig. 9 Ratio of the calorimetric and spectroscopic absorption cross sections at the laser wavelength reported by Sipkens et al. [23] for aerosols of solid molybdenum, iron, and silver nanoparticles. Rectangles represent the uncertainty in the reported values. The lighter rectangles show the original values, and the darker rectangles indicate the results when accounting for Mie theory, polydisperse particle sizes, and the change in refractive index with melting

molybdenum nanoparticles reported by Sipkens et al. [23]. Following this procedure, Fig. 9 shows that the effective absorption cross sections predicted using the spectroscopic model are generally more consistent with the calorimetrically inferred values, particularly for the aerosol of molybdenum nanoparticles. For the iron nanoparticles, accounting for Mie theory, the change in refractive index upon melting, and polydisperse sizes in the spectroscopic cross section brings it closer to the calorimetric cross section, but the calorimetric cross section is still larger by a factor of 2–3. This indicates that the effective temperature reached by the aerosol during the LII measurements is higher than the one predicted by the simulation using the most accurate physical model. This remaining discrepancy may suggest that the nanoparticle size distribution is larger than what Sipkens et al. [23] measured by dynamic light scattering. It is also possible that the aerosol contained aggregates, as opposed to isolated nanospheres, which would affect both the spectroscopic and heat transfer models. Rayleigh–Debye–Gans fractal aggregate (RDG-FA) theory does not apply to these aggregates because it is fundamentally dependent on primary particles to be in the Rayleigh regime. For aggregates, multiple internal scattering may increase the overall absorption efficiency of the aggregate compared to the individual nanoparticles [60–63]. Semi-analytical methods such as discrete dipole approximation (DDA) [64–66] or T-matrix [63, 67, 68] or fully numerical schemes such as finite-different time-domain (FDTD) [69] can be used to retrieve optical properties of aggregates. Due to the heat-up, the aggregates will go through a sintering process which will change their morphology during the measurements [70, 71]. Partial oxidation of the nanoparticle could also increase the absorption cross section due to constructive electromagnetic field interference [72]. Alternatively, the uncertainty in Clausius–Clapeyron equation prediction of vapour partial pressure may be contributing to the remaining discrepancies [20]. In the case of Mo nanoparticles, due to high melting temperature (~2896 K), no evaporation occurs and the discrepancy is completely solved after applying the Mie theory and polydispersity.

For the silver nanoparticles, accounting for Mie theory, polydispersity, and the change in refractive index lowers the ratio of calorimetrically to spectroscopically defined absorption efficiencies from 16.4 ± 0.72 to 10.1 ± 0.45. The large ratio is a consequence of the relatively small absorption cross section of silver nanoparticles. In principle, it should not be possible for the laser pulse to heat the silver

nanoparticles more than 100 K above their initial temperature at the given fluences. This suggests that other phenomena may be involved (e.g., the observed signals are not incandescence, but some other non-incandescent phenomena [36]).

4.5 Spectral distribution of $E(m_\lambda)$ for iron nanoparticles

Finally, we consider the discrepancy between the experimentally implied and spectroscopically derived values of $E(m)_r$, which is defined as

$$E(m)_r \equiv \frac{E\left(m_{\lambda_1}\right)}{E\left(m_{\lambda_2}\right)}. \tag{38}$$

As expected, the $E(m)_r$ from Rayleigh theory is independent of particle size. In contrast, the equivalent $E(m)_r$ calculated by Mie theory depends on particle size,

$$E(m)_{r,\mathrm{Mie}} = \frac{\lambda_2\left(Q_{\mathrm{abs},\lambda 1}\right)}{\lambda_1\left(Q_{\mathrm{abs},\lambda 2}\right)} \tag{39}$$

Sipkens et al. [23] estimated an experimentally implied value of $E(m)_r$ by assuming that the plateau in the peak effective temperature for higher fluences should only slightly exceed the boiling point of the material, T_{boil}. Under this assumption, the value of $E(m)_r$ implied by the experiments can be approximated as

$$\left[E(m)_r\right]_{\mathrm{exp}} \approx \frac{J_{\lambda 1}(t)}{J_{\lambda 2}(t)}\left(\frac{\lambda_1}{\lambda_2}\right)^6 \exp\left[-\frac{hc_0}{k_B}\left(\frac{1}{\lambda_2}-\frac{1}{\lambda_1}\right)\frac{1}{T_{\mathrm{boil}}}\right]. \tag{40}$$

Using the boiling temperature of bulk iron ($T_{\mathrm{b}} \approx 3073$ K), Sipkens et al. found $[E(m)_r]_{\mathrm{exp}} \approx 1.1$. This value is consistent with the assumption that $E(m)_r = 1.0$, which was universally adopted in previous LII studies on iron nanoparticles (e.g., Ref. [14]). However, such a value is inconsistent with the value of $E(m)_r = 1.82$ derived from the literature, cf. Table 1. The $E(m)_{r,\mathrm{Mie}}$ approaches unity for nanoparticles larger than 50 nm, cf. Fig. 10; therefore, the discrepancy might be due to the faulty assumption of Rayleigh theory.

Of course, if Rayleigh theory cannot be applied, $E(m)_r$ loses its physical meaning. In this case, one can attempt to reproduce this anomaly by defining an $[E(m)_r]_{\mathrm{sim}}$ by combining Eq. (40) with simulated incandescence that incorporates Mie theory, polydispersity and the change in the refractive index due to melting. Simulated TiRe-LII measurements for iron nanoparticles are generated for this purpose using the experimental parameters reported by Sipkens et al. [23] ($d_{\mathrm{p,g}} = 40$ nm, $\sigma_{\mathrm{p,g}} = 1.16$) at a fluence of $F_0 = 2.9$ mJ/mm^2. Following this procedure results in $[E(m)_r]_{\mathrm{sim}} = 11.17$. The magnitude of this value, which greatly exceeds what could be considered plausible, stems from the fact that $[E(m)_r]_{\mathrm{sim}}$ must significantly enhance the incandescence from the nanoparticles, which only reach $T_{\mathrm{peak}}^{\mathrm{eff,Rayl}} = 1795$ K, to match the emission expected from nanoparticles at the boiling point ($T_{\mathrm{boil}} = 3073$ K) used in Eq. (40).

To proceed, then, we next consider that the excessive absorption by the nanoparticle can be accommodated by artificially modifying $Q_{\mathrm{abs},\lambda}^{\mathrm{Mie}}(d_{\mathrm{p}})$ to $yQ_{\mathrm{abs},\lambda}^{\mathrm{Mie}}(d_{\mathrm{p}})$, where y coefficient accounts for some unknown mechanism that could modify the absorption. Figure 11 shows that as y increases, the value of $T^{\mathrm{eff,Rayl}}$ increases to T_{boil} and $[E(m)_r]_{\mathrm{sim}}$ decreases to the value inferred by Sipkens et al. [23] (in fact, dropping below 1.1). This suggests that, if the excessive absorption is assumed to be physical, the difference between the spectroscopic value of $E(m)_r$ and the experimental $[E(m)_r]_{\mathrm{exp}}$ from Sipkens et al. [23] could stem from a misapplication of Rayleigh theory. This is to say that the combination of: (1) Mie theory causing a distribution of nanoparticle temperatures; (2) these temperatures being weighted more heading towards the larger, hotter particles (cf. Fig. 5); and (3) the inadequacy of Eq. (39) and using a single nanoparticle temperature to infer a value of $E(m)_r$ combine to suppress the perceived value of $[E(m)_r]_{\mathrm{exp}}$.

Another possibility is that there is no need to artificially modify $Q_{\mathrm{abs},\lambda}^{\mathrm{Mie}}(d_{\mathrm{p}})$ to reach lower values of $[E(m)_r]_{\mathrm{sim}}$, but the size distribution differs from the ex situ characterization. This could lead to higher nanoparticle temperatures, and therefore a lower $[E(m)_r]_{\mathrm{sim}}$. Figure 12 shows a contour plot of $[E(m)_r]_{\mathrm{sim}}$ as a function of $d_{\mathrm{p,g}}$ and the geometric standard deviation, $\sigma_{\mathrm{p,g}}$, respectively, for a fixed fluence of $F_0 = 2.9$ mJ/mm^2. The results show that a value of 1.21 is reached only for

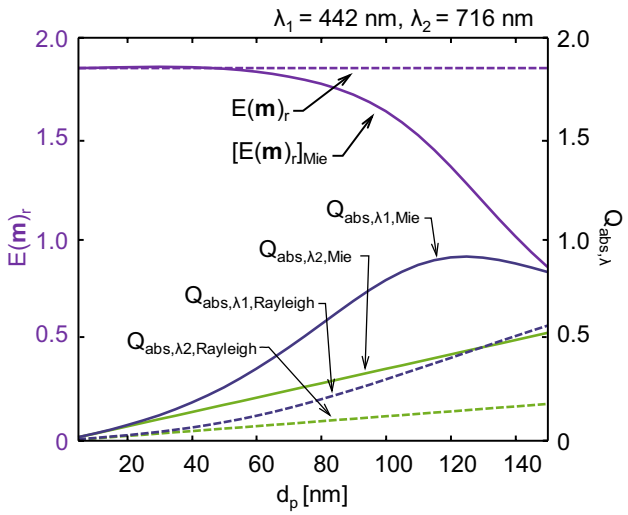

Fig. 10 Comparing Rayleigh and Mie absorption at 442 nm and 716 nm for liquid iron nanoparticles

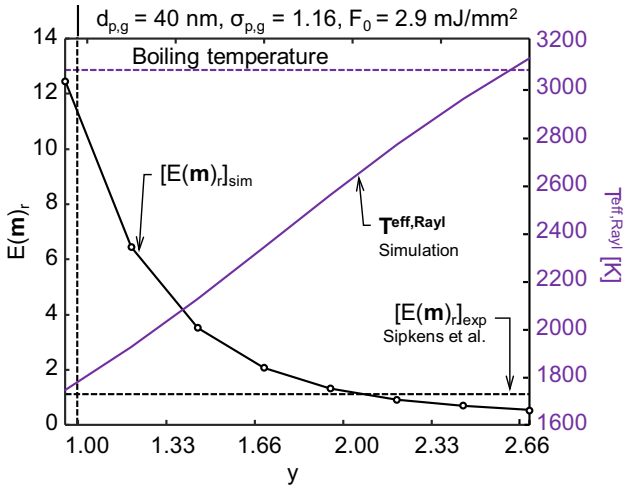

Fig. 11 Comparison of $[E(m)_r]_{sim}$, which is inferred from simulations, as a function of y coefficient for the size distribution reported by Sipkens et al. [23] ($d_{p,g}$ = 40 nm, $\sigma_{p,g}$ = 1.16) to $[E(m)_r]_{exp}$ inferred from experimental data at F_0 = 2.9 mJ/mm²

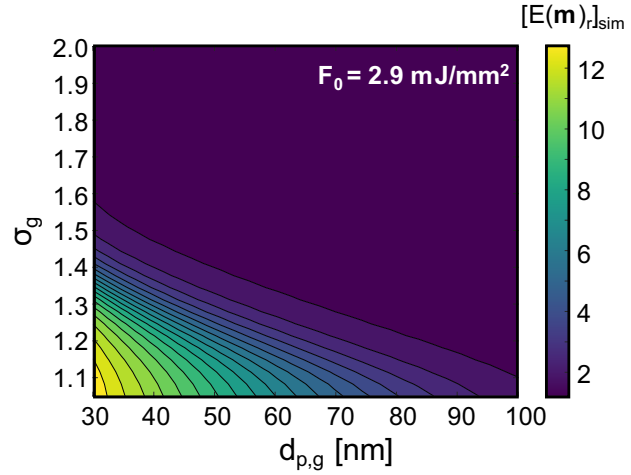

Fig. 12 Simulation results as a function of $d_{p,g}$ and $\sigma_{p,g}$ for a fixed value of laser fluence. The minimum value of $[E(m)_r]_{sim}$ is 1.21 in the figure

extreme values of $d_{p,g}$ and $\sigma_{p,g}$, which is significantly different from the DLS size distribution reported by Sipkens et al. [23]. Accordingly, this scenario is less likely.

4.6 Effect of nanoparticle charge

The Mie scattering coefficients in Eqs. (17) and (18) are derived by solving the Helmholtz wave equation for a non-charged and non-magnetic sphere suspended in a non-absorbing medium [53, 54]. During the LII experiments, we expect the nanoparticles to accumulate a positive charge due to electron emission processes [37, 73, 74]. The synthesis process can also impart a charge on the nanoparticles. In the case of a nanoparticle colloid, for example, synthesis surfactants are used to protect the surface of the nanoparticles, stop their growth and prevent agglomeration by adding a positive or negative net charge to the nanoparticle [75].

In the case of a non-magnetic charged nanoparticle, the modified Mie scattering coefficients are [76–78]

$$a_l = \frac{u\psi_l(uy)\psi_l'(y) - \psi_l(y)\psi_l'(uy) + gu\psi_l'(uy)\psi_l'(y)}{u\psi_l(uy)\xi_l'(y) - \xi_l(y)\psi_l'(uy) + gu\psi_l'(uy)\xi_l'(y)}, \tag{41}$$

and

$$b_l = \frac{\psi_l(uy)\psi_l'(y) - u\psi_l(y)\psi_l'(uy) - gu\psi_l(y)\psi_l(uy)}{\psi_l(uy)\xi_l'(y) - u\xi_l(y)\psi_l'(uy) - gu\xi_l(y)\psi_l(uy)}, \tag{42}$$

where

$$g = -\frac{f_c|\Phi|}{x_p}\frac{\omega}{\omega + j\gamma_s}. \tag{43}$$

In Eq. (43) Φ is the electrostatic potential of the nanoparticle in volts defined as

$$\Phi = \frac{N_e e_{elec}}{2\pi\varepsilon_o d_p}\mathrm{sgn}(N_e), \tag{44}$$

where N_e is integer charge of the nanoparticle, e_{elec} is electron charge, sgn(·) is the signum function, $f_c = \varepsilon_0\mu_0 e_{elec}/m_{elec} = 1.96\times10^{-6}$, and the parameters $\gamma_s \approx 2\pi k_B T_p/h$ [79, 80], h and k_B are Planck and Boltzmann constants, respectively. As shown in Eq. (44), the charge–size ratio of the nanoparticle alters the Mie scattering coefficients compared to the non-charged ones.

We consider absorption efficiencies calculated using the exact Mie coefficients, Eqs. (41) and (42), as well as an approximation by Wang et al. [79] for 442 nm, 716 nm and 1064 nm as a function of the nanoparticle charge and at T_p = 2000 K. Mitrani et al. [73] predicted a maximum of N_e = 40 for carbonaceous nanoparticles through thermionic emission during TiRe-LII experiments. Talebi-Moghaddam et al. [36] predicted a maximum value of N_e = 12 for liquid silicon nanoparticle. In all cases, our calculations show that the nanoparticle charge has a negligible impact on the absorption efficiency.

5 Conclusions

Time-resolved laser-induced incandescence is increasingly applied to measure metal nanoparticles, but there remain several anomalies that cannot be explained using standard

LII models. Instead, a number of effects have been speculated in the literature, including size-dependent optical properties and signal contamination by non-incandescent laser-induced emission (e.g., from a plasma). Our analysis showed that many of these discrepancies, including temporal variation in the intensity scaling factor during TiRe-LII measurements on molten (metal) silicon, enhanced absorption cross sections of molybdenum and iron nanoparticles, and the $[E(m)_r]_{\mathrm{exp}}$ ratio for iron nanoparticles, can be partially explained by: (1) the fact that the Rayleigh approximation of Mie theory is usually invalid for metal nanoparticles under TiRe-LII conditions; (2) polydisperse particle sizes, coupled with Mie theory, increase temperature non-uniformity in the aerosol; (3) and the fact that the radiative properties of iron change significantly upon melting. Our analysis also shows that the charge state of metal nanoparticles is unlikely to contribute to these phenomena.

While implementing Mie theory explains some of the observed anomalies, some problems remain. For example, the spectroscopically defined absorption cross section of silver nanoparticles restricts nanoparticle heating to only several hundred Kelvin, which would render incandescence undetectable. Also, in the case of iron nanoparticles, while the discrepancy between calorimetrically and spectroscopically derived absorption cross sections has been reduced, it has not been eliminated fully. This may be connected to the discrepancy in the $E(m)_r$ value for iron nanoparticles, which is not completely explained by the faulty assumptions of Rayleigh approximation and monodisperse sizes. These results point to other deficiencies in the spectroscopic model, such as non-incandescent LIE contaminating the incandescence signals, uncertainty in the physical parameters used in the simulation, oxidation, or aggregation and sintering effects for iron nanoparticles. These factors will be the focus of future work.

Acknowledgements This research was supported by the Natural Science and Engineering Research Council Discovery Grant (RGPIN-2018-03756) and the Killam Foundation (Postdoctoral Fellowship). This research was enabled in part by support provided by (SHARCNET) (www.sharcnet.ca) and Compute Canada (www.computecanada.ca).

References

1. F.E. Kruis, H. Fissan, A. Peled, J. Aerosol Sci. **29**, 511 (1998)
2. Y.L. Luo, Y.S. Shiao, Y.F. Huang, ACS Nano **5**, 7796 (2011)
3. D.P. O'Neal, L.R. Hirsch, N.J. Halas, J.D. Payne, J.L. West, Cancer Lett. **209**, 171 (2004)
4. H.X. Xu, E.J. Bjerneld, M. Käll, L. Börjesson, Phys. Rev. Lett. **83**, 4357 (1999)
5. H.A. Atwater, A. Polman, Nat. Mater. **9**, 205 (2010)
6. S.K. Sahoo, S. Parveen, J.J. Panda, Nanomedicine **3**, 20 (2007)
7. T. L. Thiem, Y.-I. I. Lee, and J. Sneddon, *Lasers in Atomic Spectroscopy: Selected Applications* (Elsevier B.V., 1992), pp. 1–35
8. M.A. Maurer-Jones, I.L. Gunsolus, C.J. Murphy, C.L. Haynes, Anal. Chem. **85**, 3036 (2013)
9. L.A. Melton, Appl. Opt. **23**, 2201 (1984)
10. R.W. Weeks, W.W. Duley, J. Appl. Phys. **45**, 4661 (1974)
11. H.A. Michelsen, C. Schulz, G.J. Smallwood, S. Will, Prog. Energy Combust. Sci. **51**, 2 (2015)
12. R.L. Vander Wal, T.M. Ticich, J.R. West, Appl. Opt. **38**, 5867 (1999)
13. A.V. Filippov, M.W. Markus, P. Roth, J. Aerosol Sci **30**, 71 (1999)
14. R. Starke, B. Kock, P. Roth, Shock Waves **12**, 351 (2003)
15. E.V. Gurentsov, A.V. Eremin, High Temp. **49**, 667 (2011)
16. T. Sipkens, G. Joshi, K.J. Daun, Y. Murakami, J. Heat Transfer **135**, 052401 (2013)
17. T.A. Sipkens, P.J. Hadwin, S.J. Grauer, K.J. Daun, Appl. Opt. **56**, 8436 (2017)
18. G.S. Eom, C.W. Park, Y.H. Shin, K.H. Chung, S. Park, W. Choe, J.W. Hahn, Appl. Phys. Lett. **83**, 1261 (2003)
19. T.A. Sipkens, R. Mansmann, K.J. Daun, N. Petermann, J.T. Titantah, M. Karttunen, H. Wiggers, T. Dreier, C. Schulz, Appl. Phys. B Lasers Opt. **116**, 623 (2014)
20. J. Menser, K. Daun, T. Dreier, C. Schulz, Appl. Phys. B **122**, 277 (2016)
21. I.S. Altman, D. Lee, J.D. Chung, J. Song, M. Choi, Phys. Rev. B **63**, 161402 (2001)
22. S. Maffi, S. De Iuliis, F. Cignoli, G. Zizak, Appl. Phys. B Lasers Opt. **104**, 357 (2011)
23. T.A. Sipkens, N.R. Singh, K.J. Daun, Appl. Phys. B Lasers **123**, 14 (2017)
24. A. Eremin, E. Gurentsov, E. Popova, K. Priemchenko, Appl. Phys. B Lasers Opt. **104**, 285 (2011)
25. B.F. Kock, C. Kayan, J. Knipping, H.R. Orthner, P. Roth, Proc. Combust. Inst. **30**, 1689 (2005)
26. T.A. Sipkens, J. Menser, R. Mansmann, C. Schulz, K.J. Daun, Appl. Phys. B **125**, 140 (2019)
27. T. A. Sipkens, Advances in the Modeling of Time-Resolved Laser-Induced Incandescence, University of Waterloo, 2018
28. F. Migliorini, S. De Iuliis, S. Maffi, G. Zizak, Appl. Phys. B Lasers Opt. **120**, 417 (2015)
29. F. Liu, S. Rogak, D.R. Snelling, M. Saffaripour, K.A. Thomson, G.J. Smallwood, Appl. Phys. B Lasers Opt. **122**, 1 (2016)
30. L.B. Scaffardi, J.O. Tocho, Nanotechnology **17**, 1309 (2006)
31. G. Bisker, D. Yelin, J. Opt. Soc. Am. B **29**, 1383 (2012)
32. C.R. Shaddix, K.C. Smyth, Combust. Flame **107**, 418 (1996)
33. A.J. Fernandez, M.A. Shannon, R.E. Russo, X.L. Mao, Appl. Spectrosc. **49**, 1054 (1995)
34. A.M. Brown, R. Sundararaman, P. Narang, W.A. Goddard, H.A. Atwater, ACS Nano **10**, 957 (2015)
35. T. Haug, P. Klemm, S. Bange, J.M. Lupton, Phys. Rev. Lett. **115**, 067403 (2015)
36. S.T. Moghaddam, K.J. Daun, Appl. Phys. B **124**, 159 (2018)
37. R. Yen, J. Liu, N. Gloembergen, Opt. Commun. **35**, 277 (1980)
38. C. Clavero, Nat. Photonics **8**, 95 (2014)
39. T.A. Sipkens, N.R. Singh, K.J. Daun, N. Bizmark, M. Ioannidis, Appl. Phys. B Lasers Opt. **119**, 561 (2015)
40. K. Daun, J. Menser, R. Mansmann, S.T. Moghaddam, T. Dreier, C. Schulz, J. Quant. Spectrosc. Radiat. Transf. **197**, 3 (2017)
41. D.R. Snelling, K.A. Thomson, F. Liu, G.J. Smallwood, Appl. Phys. B Lasers Opt. **96**, 657 (2009)
42. T. Dreier, C. Schulz, Powder Technol. **287**, 226 (2016)
43. H.A. Michelsen, M.A. Linne, B.F. Kock, M. Hofmann, B. Tribalet, C. Schulz, Appl. Phys. B Lasers Opt. **93**, 645 (2008)
44. H.A. Michelsen, F. Liu, B.F. Kock, H. Bladh, A. Boiarciuc, M. Charwath, T. Dreier, R. Hadef, M. Hofmann, J. Reimann, S. Will, P.E. Bengtsson, H. Bockhorn, F. Foucher, K.P. Geigle, C. Mounaïm-Rousselle, C. Schulz, R. Stirn, B. Tribalet, R. Suntz, Appl. Phys. B Lasers Opt. **87**, 503 (2007)

45. H. Pan, J.A. Ritter, P.B. Balbuena, Langmuir **14**, 6323 (1998)
46. A.D. Rakic, A.B. Djurisic, J.M. Elazar, M.L. Majewski, Appl. Opt. **37**, 5271 (1998)
47. P. Johnson, R. Christy, Phys. Rev. B **9**, 5056 (1974)
48. S. Krishnan, K.J. Yugawa, P.C. Nordine, Phys. Rev. B **55**, 8201 (1997)
49. K.D. Li, P.M. Fauchet, Appl. Phys. Lett. **51**, 1747 (1987)
50. B.T. Barnes, J. Opt. Soc. Am. **56**, 1546 (1966)
51. J.C. Miller, Philos. Mag. **20**, 1115 (1969)
52. H. Kobatake, H. Fukuyama, Metall. Mater. Trans. A **47**, 3303 (2016)
53. G. Mie, Ann. Phys. **330**, 377 (1908)
54. C.F. Bohren, D.R. Huffman, *Absorption and Scattering of Light by Small Particles* (Wiley, Hoboken, 1983)
55. W.H. Dalzell, A.F. Sarofim, J. Heat Transfer **91**, 100 (1969)
56. C.M. Sorensen, J.B. Maughan, H. Moosmüller, J. Quant. Spectrosc. Radiat. Transf. **226**, 81 (2019)
57. D. Schebarchov, B. Auguié, E.C. Le Ru, Phys. Chem. Chem. Phys. **15**, 4233 (2013)
58. C. Schulz, B.F. Kock, M. Hofmann, H. Michelsen, S. Will, B. Bougie, R. Suntz, G. Smallwood, Appl. Phys. B **83**, 333 (2006)
59. P.J. Hadwin, T.A. Sipkens, K.A. Thomson, F. Liu, K.J. Daun, Appl. Phys. B **122**, 1 (2016)
60. C.M. Sorensen, Light scattering by fractal aggregates: a review. Aerosol Sci. Technol. **35**, 648–687 (2001)
61. S.T. Moghaddam, H. Ertürk, M.P. Mengüç, J. Quant. Spectrosc. Radiat. Transf. **178**, 124 (2016)
62. S.T. Moghaddam, D. Avşar, H. Ertürk, M.P. Mengüç, J. Quant. Spectrosc. Radiat. Transf. **197**, 106 (2017)
63. S.T. Moghaddam, P.J. Hadwin, K.J. Daun, J. Aerosol Sci. **111**, 36 (2017)
64. E.M. Purcell, C.R. Pennypacker, Astrophys. J. **186**, 705 (1973)
65. B.T. Draine, P.J. Flatau, J. Opt. Soc. Am. A **11**, 1491 (1994)
66. D. Avşar, H. Ertürk, M.P. Mengüç, Mater. Res. Express **6**, 065006 (2019)
67. D.W. Mackowski, M.I. Mishchenko, JOSA A **13**, 2266 (1996)
68. D.W. Machowski, M.I. Mishchenko, J. Quant. Spectrosc. Radiat. Transf. **112**, 2182 (2013)
69. G. Mur, I.E.E.E. Trans, Electromagn. Compat. EMC **23**, 377 (1981)
70. M.L. Eggersdorfer, D. Kadau, H.J. Herrmann, S.E. Pratsinis, Langmuir **27**, 6358 (2011)
71. N.L. Peterson, J. Nucl. Mater. **69–70**, 3 (1978)
72. H. Suzuki, S.I. Yin, Int. J. Phys. Sci. **3**, 38 (2008)
73. J.M. Mitrani, M.N. Shneider, B.C. Stratton, Y. Raitses, Appl. Phys. Lett. **108**, 054101 (2016)
74. R. Sundararaman, P. Narang, A.S. Jermyn, W.A. Goddard, H.A. Atwater, Nat. Commun. **5**, 5788 (2014)
75. A. Gole, C.J. Murphy, Chem. Mater. **16**, 3633 (2004)
76. C.F. Bohren, A.J. Hunt, Can. J. Phys. **55**, 1930 (1977)
77. J. Klacka, M. Kocifaj, J. Quant. Spectrosc. Radiat. Transf. **106**, 170 (2007)
78. X. Li, L. Xie, X. Zheng, J. Quant. Spectrosc. Radiat. Transf. **113**, 251 (2012)
79. N. Wang, S. Liu, Z. Lin, Opt. Express **21**, 20387 (2013)
80. J. Klacka, M. Kocifaj, Prog. Electromagn. Res. **109**, 17 (2010)